Mon. Not. R. Astron. Soc. **000**, 000–000 (0000) Printed 6 March 2022 (MN LATEX style file v2.2)

Are pulsars born with a hidden magnetic field?

Alejandro Torres-Forné[1⋆], Pablo Cerdá-Durán[1], José A. Pons[2] and José A. Font[1,3]
[1]*Departamento de Astronomía y Astrofísica, Universitat de València, Dr. Moliner 50, 46100, Burjassot (València), Spain*
[2]*Departament de Física Aplicada, Universitat d'Alacant, Ap. Correus 99, 03080 Alacant, Spain*
[3]*Observatori Astronòmic, Universitat de València, Catedrático José Beltrán 2, 46980, Paterna (València), Spain*

arXiv:1511.03823v2 [astro-ph.SR] 11 Dec 2015

6 March 2022

ABSTRACT
The observation of several neutron stars in the center of supernova remnants and with significantly lower values of the dipolar magnetic field than the average radio-pulsar population has motivated a lively debate about their formation and origin, with controversial interpretations. A possible explanation requires the slow rotation of the proto-neutron star at birth, which is unable to amplify its magnetic field to typical pulsar levels. An alternative possibility, the hidden magnetic field scenario, considers the accretion of the fallback of the supernova debris onto the neutron star as responsible for the submergence (or screening) of the field and its apparently low value. In this paper we study under which conditions the magnetic field of a neutron star can be buried into the crust due to an accreting, conducting fluid. For this purpose, we consider a spherically symmetric calculation in general relativity to estimate the balance between the incoming accretion flow and the magnetosphere. Our study analyses several models with different specific entropy, composition, and neutron star masses. The main conclusion of our work is that typical magnetic fields of a few times 10^{12} G can be buried by accreting only $10^{-3} - 10^{-2} M_\odot$, a relatively modest amount of mass. In view of this result, the Central Compact Object scenario should not be considered unusual, and we predict that anomalously weak magnetic fields should be common in very young ($<$ few kyr) neutron stars.

Key words: stars: magnetic field – stars: neutron – pulsars: general

1 INTRODUCTION

Central Compact Objects (CCOs) are isolated, young neutron stars (NSs) which show no radio emission and are located near the center of young supernova remnants (SNRs). Three such NSs, PSR E1207.4-5209, PSR J0821.0-4300, and PSR J1852.3-0040, show an inferred magnetic field significantly lower than the standard values for radio-pulsars (i.e. 10^{12} G). The main properties of these sources are summarized in Table 1. In all cases, the difference between the characteristic age of the neutron star $\tau_c = P/\dot{P}$ and the age of the SNR indicates that these NSs were born spinning at nearly their present periods ($P \sim 0.1 - 0.4$ s). This discovery has challenged theoretical models of magnetic field generation, that need to be modified to account for their peculiar properties.

The first possible explanation for the unusual magnetic field found in these objects simply assumes that these NSs are born with a magnetic field much lower than that of their classmates. This value can be amplified by turbulent dynamo action during the proto-neutron star (PNS) phase (Thompson & Duncan 1993; Bonano et al. 2005) . In this model, the final low values of the magnetic field would reflect the fact that the slow rotation of the neutron star at birth does not suffice to effectively amplify the magnetic field through dynamo effects. However, recent studies have shown that, even in the absence of rapid rotation, magnetic fields in PNS can be amplified by other mechanisms such as convection and the standing accretion shock instability (SASI) (Endeve et al. 2012; Obergaulinger et al. 2014).

An alternative explanation is the hidden magnetic field scenario (Young & Chanmugan 1995; Muslimov & Page 1995; Geppert et al. 1999; Shabaltas & Lai 2012). Following the supernova explosion and the neutron star birth, the supernova shock travels outwards through the external layers of the star. When this shock crosses a discontinuity in density, it is partially reflected and moves backwards (reverse shock). The total mass accreted by the reverse shock in this process is in the range from $\sim 10^{-4} M_\odot$ to a few solar masses on a typical timescale of hours to days (Ugliano et al. 2012). Such a high accretion rate can compress the magnetic field of the NS which can eventually be buried into the neutron star crust. As a result, the value of the external magnetic field would be significantly lower than the internal 'hidden' magnetic field. Bernal et al. (2010) performed 1D and 2D numerical simulations of a single column of material falling onto a magnetized neutron star and showed how the magnetic field can be buried into the neutron star crust.

Once the accretion process stops, the magnetic field might eventually reemerge. The initial studies investigated the process of reemergence using simplified 1D models and dipolar fields (Young

⋆ E-mail: Alejandro.Torres@uv.es

Table 1. Central Compact Objects in Supernova Remnants. From left to right the columns indicate the name of the CCO, the age, the distance d, the period P, the inferred surface magnetic field, $\mathrm{B_s}$, the bolometric luminosity in X-rays, $\mathrm{L_{x,bol}}$, the name of the remnant, the characteristic age, and bibliographical references.

CCO	Age (kyr)	d (kpc)	P (s)	$\mathrm{B_s}$ 10^{11}G	$\mathrm{L_{x,bol}}$ (erg $\mathrm{s^{-1}}$)	SNR	τ_c (Myr)	References
J0822.0-4300	3.7	2.2	0.112	0.65	6.5×10^{33}	Puppis A	190	1, 2
1E 1207.4-5209	7	2.2	0.424	2	2.5×10^{33}	PKS 1209-51/52	310	2, 3, 4, 5, 6, 7
J185238.6 + 004020	7	7	0.105	0.61	5.3×10^{33}	Kes 79	190	8, 9, 10, 11

References: (1) Hui & Becker (2006), (2) Gotthelf & Halpern (2013), (3) Zavlin et al. (2000), (4) Mereghetti et al. (2002), (5) Bignami et al. (2003), (6) De Luca et al. (2004), (7) Gotthelf & Halpern (2007), (8) Seward et al. (2003), (9) Gotthelf et al. (2005), (10) Halpern et al. (2003), (11) Halpern & Gotthelf (2010)

& Chanmugan 1995; Muslimov & Page 1995; Geppert et al. 1999) and established that the timescale for the magnetic field reemergence is $\sim 1 - 10^7$ kyr, critically depending on the depth at which the magnetic field is buried. More recent investigations have confirmed this result. Ho (2011) observed similar timescales for the reemergence using a 1D cooling code. Viganò & Pons (2012) carried out simulations of the evolution of the interior magnetic field during the accretion phase and the magnetic field submergence phase.

In the present work we study the feasibility of the hidden magnetic field scenario using a novel numerical approach based on the solutions of 1D Riemann problems (discontinuous initial value problems) to model the compression of the magnetic field of the NS. The two initial states for the Riemann problem are defined by the magnetosphere and by the accreting fluid, at either sides of a moving, discontinuous interface. Following the notation defined in Michel (1977), the NS magnetosphere refers to the area surrounding the star where the magnetic pressure dominates over the thermal pressure of the accreting fluid. The magnetopause is the interface between the magnetically dominated area and the thermally dominated area. The equilibrium point is defined as the radius at which the velocity of the contact discontinuity is zero.

The paper is organized as follows. In Sections 2 to 5 we present the model we use to perform our study. We describe in these sections the equation of state (EoS) of the accreting fluid, the spherically symmetric Michel solution characterizing the accreting fluid, and all the expressions needed to compute the potential solution for the magnetic field in the magnetosphere. Section 6 contains the main results of this work. After establishing a reference model, we vary the remaining parameters, namely entropy, composition and the initial distribution of the magnetic field, and study their influence on the fate of the magnetic field. Finally, in Section 7 we summarize the main results of our study and present our conclusions and plans for future work. If not explicitly stated otherwise we use units of $G = c = 1$. Greek indices ($\mu, \nu \ldots$) run from 0 to 3 and latin indices ($i, j \ldots$) form 1 to 3.

2 THE REVERSE SHOCK AND THE FALLBACK SCENARIO.

At the end of their lives, massive stars ($M_{\rm star} \gtrsim 8 M_\odot$) possess an onion-shell structure as a result of successive stages of nuclear burning. An inner core, typically formed by iron, with a mass of $\sim 1.4 M_\odot$ and ~ 1000 km radius develops at the centre, balancing gravity through the pressure generated by a relativistic, degenerate, $\gamma = 4/3$, fermion gas. The iron core is unstable due to photo-disintegration of nuclei and electron captures, which result in a deleptonization of the core and a significant pressure reduction ($\gamma < 4/3$). As a result, the core shrinks and collapses gravitationally to nuclear matter densities on dynamical timescales (~ 100 ms). As the center of the star reaches nuclear saturation density ($\sim 2 \times 10^{14}$ g cm^{-3}), the EoS stiffens and an outward moving (prompt) shock is produced. As it propagates out the shock suffers severe energy losses dissociating Fe nuclei into free nucleons ($\sim 1.7 \times 10^{51}$ erg$/0.1 M_\odot$), consuming its entire kinetic energy inside the iron core (it stalls at $\sim 100 - 200$ km), becoming a standing accretion shock in a few ms. There is still debate about the exact mechanism and conditions for a successful explosion, but it is commonly accepted that the standing shock has to be revived on a timescale of $\lesssim 1$ s by the energy deposition of neutrinos streaming out of the innermost regions, and some form of convective transport for the shock to carry sufficient energy to disrupt the whole star (see Janka et al. 2007, for a review on the topic).

Even if the shock is sufficiently strong to power the supernova, part of the material between the nascent neutron star and the propagating shock may fall back into the neutron star (Colgate 1971; Chevalier 1989). Determining the amount of fallback material depends not only on the energy of the shock but also on the radial structure of the progenitor star (Fryer 2006). Most of the fallback accretion is the result of the formation of an inward moving reverse shock produced as the main supernova-driving shock crosses the discontinuity between the helium shell and the hydrogen envelope (Chevalier 1989). For typical supernova progenitors ($10-30\ M_\odot$) the base of the hydrogen envelope is at $r_{\rm H} \sim 10^{11}$ cm to 3×10^{12} cm (Woosley et al. 2002), which is reached by the main shock on a timescale of a few hours. The reverse shock travels inwards carrying mass that accretes onto the NS. It reaches the vicinity of the NS on a timescale of hours, about the same time at which the main supernova shock reaches the surface of the star (Chevalier 1989). By the time the reverse shock reaches the NS, the initially hot proto-neutron star has cooled down significantly. In its first minute of life the PNS contracts, cools down to $T < 10^{10}$ K and becomes transparent to neutrinos (Burrows & Lattimer 1986; Pons et al. 1999). In the next few hours the inner crust ($\rho \in [2 \times 10^{11}, 2 \times 10^{14}]$ g cm^{-3}) solidifies but the low density envelope ($\rho < 2 \times 10^{11}$ g cm^{-3}), which will form the outer crust on a timescale of $1 - 100$ yr, remains fluid (Page et al. 2004; Aguilera et al. 2008).

Understanding the processes generating the magnetic field observed in NSs, in the range from $\sim 10^{10}$ G to $\sim 10^{15}$ G, is still a open issue. Most likely, convection, rotation and turbulence during the PNS phase play a crucial role in field amplification (Thompson & Duncan 1993). However, at the time in the evolution that we

are considering (hours after birth), none of these processes can be active anymore and the electric current distribution generating the magnetic field will be frozen in the interior of the NS. These currents evolve now on the characteristic Hall and Ohmic timescales of 10^4-10^6 yr (Pons et al. 2007, 2009; Viganò et al. 2013), much longer than the timescale $t_{\rm acc}$ during which fallback is significant, which can be estimated as the free-fall time from the base of the hydrogen envelope

$$t_{\rm acc} \sim \frac{1}{2}\left(\frac{r_{\rm H}^3}{GM}\right)^{1/2}. \quad (1)$$

This ranges from 30 minutes to several days for the typical values of $r_{\rm H}$ and a $M = 1.4 M_\odot$.

The total mass accreted during this phase is more uncertain. Detailed 1D numerical simulations of the shock propagation and fallback estimate that typical values range from $10^{-4} M_\odot$ to a few solar masses (Woosley et al. 1995; Zhang et al. 2008; Ugliano et al. 2012). If more than a solar mass is accreted, the final outcome would be the delayed formation of a black hole, hours to days after core bounce. Chevalier (1989) and Zhang et al. (2008) showed that the accretion rate is expected to be maximum when the reverse shock reaches the NS and decreases as $t^{-5/3}$ at later times. Therefore, the total amount of accreted mass is dominated by the fallback during the first few hours. Given the theoretical uncertainties, we assume for the rest of this work that a total mass of $\delta M \in [10^{-5} M_\odot, \delta M_{\rm max}]$ is accreted during a typical timescale of $t_{\rm acc} \in [10^3, 10^4]$ s, being $\delta M_{\rm max} \sim 1 M_\odot$ the amount of mass necessary to add to the NS to form a black hole. Therefore, the typical accretion rate during fallback is $\dot{M} \in [10^{-9}, 10^{-3}] M_\odot/{\rm s}$, which, for practical purposes, we assume to stay constant during the accretion phase. This accretion rate, even at its lowest value, exceeds by far the Eddington luminosity

$$\frac{\dot{M} c^2}{L_{\rm Edd}} = 5 \times 10^6 \left(\frac{\dot{M}}{10^{-9} M_\odot/{\rm s}}\right), \quad (2)$$

with $L_{\rm Edd} = 3.5 \times 10^{38}$ erg s^{-1} the Eddington luminosity for electron scattering.

In the hypercritical accretion regime, the optical depth is so large that photons are advected inwards with the flow faster than they can diffuse outwards (Blondin 1986; Chevalier 1989; Houck et al. 1991). As a result the accreting material cannot cool down resulting in an adiabatic compression of the fluid. The dominant process cooling down the accreting fluid and releasing the energy stored in the infalling fluid is neutrino emission (Houck et al. 1991). At temperatures above the pair creation threshold, $T_{\rm pair} \approx 10^{10}$ K, pair annihilation can produce neutrino-antineutrino pairs, for which the infalling material is essentially transparent and are able to cool down very efficiently the material as it is decelerated at the surface of the NS or at the magnetopause. Therefore, the specific entropy, s, of the fallback material remains constant all through the accretion phase until it decelerates in the vicinity of the NS.

The value for s is set at the time of the reverse shock formation. Detailed 2D numerical simulations of the propagation of the shock through the star (Scheck et al 2006; Kifonidis et al. 2003, 2006) show that typical values of $s \sim 20\ k_{\rm B}/{\rm nuc}$ are found at the reverse shock. At this stage of the explosion the flow is highly anisotropic due to the Rayleigh-Taylor instability present in the expanding material and the Richtmyer-Meshkov instability at the He/H interface. Those instabilities generate substantial mixing between hydrogen and helium and even clumps of high-entropy heavier elements (from C to Ni) rising from the innermost parts of the star. Therefore, the fallback material has entropy in the range $s \sim 1 - 100\ k_{\rm B}/{\rm nuc}$ and its composition, although it is mostly helium, can contain almost any element present in the explosion. 3D simulations show qualitatively similar results regarding the entropy values and mixing (Hammer et al. 2010; Joggerst et al. 2010; Wongwathanarat et al. 2015).

Outside the NS, the expanding supernova explosion leaves behind a low density rarefaction wave which is rapidly filled by the NS magnetic field, forming the magnetosphere. For the small magnetospheric densities, the inertia of the fluid can be neglected, and the magnetosphere can be considered force-free. The fallback reverse shock propagates inwards compressing this magnetosphere. The boundary between the unmagnetized material falling back and the force-free magnetosphere, i.e. the magnetopause, can be easily compressed at long distances ($r \gtrsim 10^8$ cm) due to the large difference of the pressure of the infalling material with respect to the magnetic pressure. The dynamical effect of the magnetosphere only plays a role at $r \lesssim 10^8$ cm, i.e. inside the light cylinder for most cases. The precise radius where the magnetic field becomes dynamically relevant is estimated later in Section 5.2. Only in the case of magnetar-like magnetic fields and fast initial spin ($P \lesssim 10$ ms) this consideration is not valid, although this is not the case for CCOs.

To conclude this scenario overview, we note that the magnetospheric torques will spin-down the NS on a characteristic timescale (Shapiro & Teukolsky 2004) given by

$$\tau_c = \frac{P}{2\dot{P}} \sim 180 \left(\frac{B_p}{10^{15}{\rm G}}\right)^{-2} \left(\frac{P}{1{\rm s}}\right)^2 {\rm yr}, \quad (3)$$

for a typical NS with radius 10 km and mass $1.4 M_\odot$. B_p is the value of the magnetic field at the pole of the NS. The value of the moment of inertia is 1.4×10^{45} g cm^2. At birth, the spin period of a NS is limited by the mass-shedding limit to be $P > 1$ ms (Goussard et al. 1998). If all NSs were born with millisecond periods, purely magneto-dipolar spin-down would limit the observed period of young NSs (10^4 yr) to

$$P_{{\rm obs},10^4{\rm yr}} \lesssim 5.5 \left(\frac{B}{10^{15}{\rm G}}\right)^2 {\rm s}. \quad (4)$$

For magnetic fields $B \lesssim 1.4 \times 10^{13}$ G this criterion fails for the vast majority of pulsars and all CCOs ($P \gtrsim 0.1$ s) and therefore the measured spin period must be now very close to that hours after the onset of the supernova explosion. Detailed population synthesis studies of the radio-pulsar population clearly favor a broad initial period distribution in the range 0.1-0.5 s (Faucher-Guiguère & Kaspi 2006; Gullón et al. 2014), rather than fast millisecond pulsars. Therefore, from observational constraints, it is reasonable to assume that progenitors of pulsars (including CCOs) have spin periods of $P \sim 0.1 - 0.5$ s at the moment of fallback. For such low rotation rates, the NS can be safely considered as a spherically symmetric body and its structure can thus be computed by solving the Tolman-Oppenheimer-Volkoff (TOV) equation.

3 STATIONARY SPHERICAL ACCRETION

We model the fallback of the reverse shock as the spherically symmetric accretion of an unmagnetized relativistic fluid. The stationary solutions for this system were first obtained by Michel (1972) for the case of a polytropic EoS. Here, we extend this work to account for a general (microphysically motivated) EoS. The equations that describe the motion of matter captured by a compact object, i.e. a NS or black hole, can be derived directly from the equations of

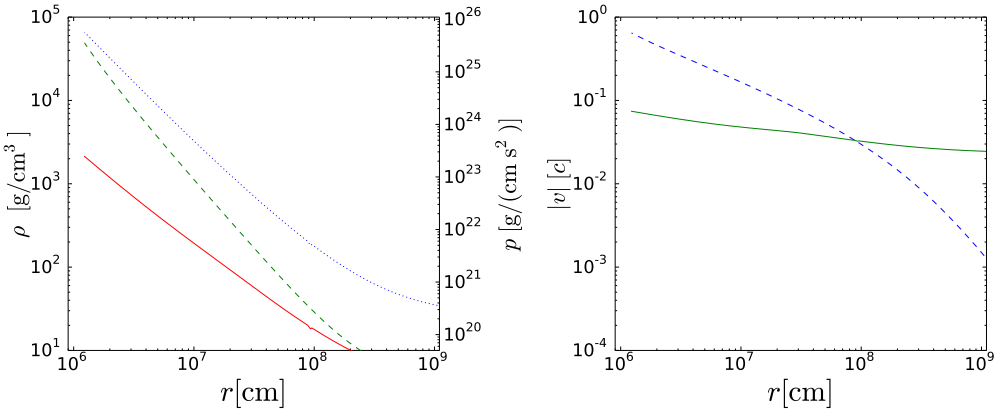


Figure 1. Illustrative accretion solution for an accretion rate $\dot{M} = 10^{-5} M_\odot/s$ and entropy per baryon $s = 80\ k_{\rm B}/{\rm nuc}$. The left panel shows the density (green-dashed line, left axis), pressure (red-solid line, right axis) and ram pressure (blue-dotted line, right axis). The right panel shows the absolute value of the fluid velocity (blue-dashed line) and the sound speed (green-solid line). The two lines cross at the critical point.

relativistic hydrodynamics , namely the conservation of rest mass,

$$\nabla_\mu J^\mu = 0\,, \tag{5}$$

and the conservation of energy-momentum,

$$\nabla_\mu T^{\mu\nu} = 0\,, \tag{6}$$

where we use the notation ∇_μ for the covariant derivative and the density current J^μ and the (perfect fluid) energy-momentum tensor $T^{\mu\nu}$ are given by

$$J^\mu = \rho u^\mu\,, \tag{7}$$
$$T_{\mu\nu} = \rho h u_\mu u_\nu + p g_{\mu\nu}\,. \tag{8}$$

In the above equations ρ is the rest-mass density, p is the pressure and h is the specific enthalpy, defined by $h = 1 + \varepsilon + p/\rho$, where ε is the specific internal energy, u^μ is the four-velocity of the fluid and $g_{\mu\nu}$ defines the metric of the general spacetime where the fluid evolves. Assuming spherical symmetry and a steady state we have

$$\frac{d}{dr}(J^1\sqrt{-g}) = 0\,, \tag{9}$$
$$\frac{d}{dr}(T^1_0\sqrt{-g}) = 0\,, \tag{10}$$

where $g \equiv \det(g_{\mu\nu})$. The exterior metric of a non-rotating compact object is given by the Schwarzschild metric

$$ds^2 = -\left(1-\frac{2M}{r}\right)dt^2 + \left(1-\frac{2M}{r}\right)^{-1}dr^2 + r^2(d\theta^2 + \sin^2\theta\, d\varphi^2)\,. \tag{11}$$

In Schwarzschild coordinates Eqs. (9) and (10) can be easily integrated to obtain (cf. Michel 1972)

$$\rho\, u\, r^2 = C_1\,, \tag{12}$$
$$h^2\left(1-\frac{2M}{r}+u^2\right) = C_2 \tag{13}$$

where C_1 and C_2 are integration constants and $u \equiv u^r$. To obtain an adiabatic solution for the accreting fluid, we differentiate Eqs. (12) and (13) at constant entropy and eliminate $d\rho$

$$\frac{du}{u}\left[V^2 - u^2\left(1-\frac{2M}{r}+u^2\right)^{-1}\right] + \frac{dr}{r}\left[2V^2 - \frac{M}{r}\left(1-\frac{2M}{r}+u^2\right)^{-1}\right] = 0\,, \tag{14}$$

where

$$V^2 \equiv \frac{\rho}{h}\left.\frac{\partial h}{\partial \rho}\right|_s\,. \tag{15}$$

The solutions of this equation are those passing through a critical point where both terms in brackets in equation (14) are zero, i.e. those fulfilling

$$2u_c^2 = \frac{M}{r_c}\,,$$
$$V_c^2 = u_c^2(1-3u_c^2)^{-1}\,, \tag{16}$$

where sub-index c indicates quantities evaluated at the critical point. The critical point can be identified as the sonic point, i.e. the point where the velocity of the fluid equals its own sound speed. After some algebra, it can be shown that the constant C_1 in equation (12) is related to the accretion rate $\dot{M}$ by

$$\dot{M} = -4\pi C_1. \tag{17}$$

Thereby we can obtain the accretion solution by simply selecting the mass accretion rate and the specific entropy of the fluid, which fixes the two constants C_1 and C_2. We note that, for each pair of values, the system (16) has two solutions, although only one represents a physical accretion solution ($|u| \to 0$ at $r \to \infty$). In this case the fluid is supersonic for radii below the critical radius and subsonic above. Figure 1 displays one illustrative accretion solution for a mass accretion rate $\dot{M} = 10^{-5} M_\odot/{\rm s}$ and entropy per baryon $s = 80 k_{\rm B}/{\rm nuc}$.

For the accreting material, we use the tabulated Helmholtz EoS (Timmes & Swesty 2000), which is an accurate interpolation of the Helmholtz free-energy of the Timmes EoS (Timmes & Arnett 1999). Timmes EoS, and Helmholtz EoS by extension, include the contributions from ionized nuclei, electrons, positrons and radiation. By default, Timmes EoS uses the rest mass density ρ [g/cm^3], temperature T [K] and composition as input. For convenience, we have developed a search algorithm that allows to call

the EoS with different thermodynamical variables as input (e.g. ρ, s and composition as inputs for the adiabatic flow of accreting material). Helmholtz EoS also requires the mean mass number $\bar{A}$ and the mean atomic number $\bar{Z}$.

At low densities, $\rho < 6 \times 10^7$ g cm^{-3}, and temperatures, $T \lesssim 2 \times 10^9$ K, nuclear reactions proceed much slower than the accretion timescale and the composition remains frozen during the accretion. We fix the composition to that at the reverse shock formation point. Given the uncertainties, we consider two possibilities in this regime, either pure helium or pure carbon. At temperatures $T \gtrsim 2 \times 10^9$ K nuclear burning becomes fast enough to change the composition. For $T \gtrsim 4 \times 10^9$ K the fluid reaches nuclear statistical equilibrium (NSE) on a significantly shorter timescale than the accretion timescale (see e.g. Woosley et al. 2002). To deal with the high temperature regime, $T \geqslant 2 \times 10^9$ K, we have tried three different approaches: 1) unchanged composition of the accreting material, 2) compute the NSE composition at a given temperature and density using a thermonuclear reaction network with 47 isotopes (Timmes 1999; Seitenzahl 2008) and 3) simplified burning with four transitions: ^{4}He for $T \leqslant 2 \times 10^9$ K, ^{56}Ni for $2 \times 10^9 > T \geqslant 5 \times 10^9$ K, ^{4}He for $5 \times 10^9 > T \geqslant 2 \times 10^{10}$ K and protons and neutrons for $T > 2 \times 10^{10}$ K. We use the publicly available routines of the Hemlholtz EoS and the NSE equilibrium kindly provided by the authors[1].

4 NON-MAGNETIZED ACCRETION AND PILE-UP

Before considering the case of magnetized accretion onto a NS, we study the case of non-magnetized accretion. For the span of accretion rates considered in this work, the sonic point of the accreted fluid is located at $r > 23500$ km at entropy $s = 10\ k_{\rm B}/{\rm nuc}$, and hence the fallback material falls supersonically onto the NS. Inevitably an accretion shock forms at the surface of the star, which propagates outwards. The accreted fluid crossing the shock will heat up, increasing its specific entropy and will fall subsonically. The high entropy of this material ($s_{shock} \in [70 - 300]\ k_{\rm B}/{\rm nuc}$) and the compression that experiments as it flows inwards raises the temperature beyond the pair creation threshold, $T_{\rm pair} \approx 10^{10}$ K, and the fluid will cool efficiently via neutrino-antineutrino annihilation. Therefore, the kinetic energy of the supersonically accreting fluid is mostly transformed into thermal energy as it crosses the accretion shock and then is dissipated to neutrinos close to the NS surface. Chevalier (1989) showed that the accretion shock will eventually stall at a certain radius as an energy balance is found. The radius of the stalled shock depends only on the accretion rate $\dot{M}$ and is located at about $R_{\rm shock} \sim 10^7 - 10^8$ km. In some estimates bellow in this work we use the values provided in table 1 in Houck et al. (1991), based in a more realistic treatment of the accretion and neutrino cooling.

The final fate of the neutrino-cooled material falling steadily onto the NS surface is to pile up on top of the original NS material forming a layer of new material. In order to study the effect of the pile up we consider a NS of mass M and radius R. If we add a mass δM to the equilibrium model, the new NS will have a new radius $R_{\rm new}$ smaller than the original one. The original surface of the star, will now be buried at a depth δR, i.e. the new surface will be located at a distance δR over the old surface. Although trivial, the last statement is important because most of the discussion below in this work is carried out in terms of δR and in terms of distances with respect to the original NS surface. Therefore it makes sense to try to compute what is the dependence of the burial depth, δR, with the total accreted mass, δM. In order to compute this dependence we use the TOV equations to solve a sequence of NS equilibrium models starting with M and progressively increasing to $M + \delta M$ for different values of δM. For each model in the sequence we compute δR as the distance between the radius enclosing a mass M and the surface of the star, i.e. the radius enclosing $M + \delta M$. Given the small values of δM, we integrate the TOV equations using a simple forward Euler method, with a step limited to relative variations of density of 10^{-5} and a maximum step of 10 cm. We have computed the relation between δR and δM for four different NS masses, $M = 1.2$, 1.4, 1.6, 1.8 and $2.0 M_\odot$. We have used several realistic EoS in tabulated form, namely four different combinations using either EoS APR (Akmal et al. 1998) or EoS L (Pandharipande et al 1997) for the core and EoS NV (Negele & Vautherin 1973) or EoS DH (Douchin & Haensel 2001) for the crust. For each case we compute the sequence up to the maximum mass; beyond that mass, the equilibrium model is unstable and it will collapse to a black hole in dynamical timescales. All EoS allow for equilibrium solutions with maximum mass consistent with recent observations of a NS with mass close to $2 M_\odot$ (Demorest et al. 2010; Antoniadis et al. 2013). The blue solid line in Fig. 2 shows the dependence of δR with δM for a $1.4 M_\odot$ NS with the APRDH EoS. All other EoS and neutron star masses show similar behavior. For all EoS, any amount of accreted mass larger than $\sim 10^{-4} M_\odot$ will sink the original NS surface to the inner crust, and for $\delta M \sim 0.1 M_\odot$ the entire crust is formed by newly accreted material. The bottom line is that, if the accreted material is able to compress the magnetosphere and deposit itself on top of the NS,

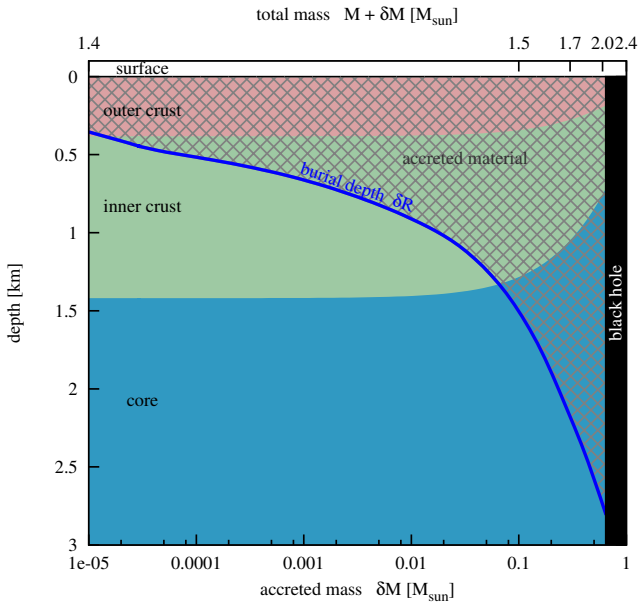


Figure 2. Dependence of the burial depth (blue solid lines), δR, with the accreted mass, δM (bottom axis), for a $M = 1.4 M_\odot$ NS using APRDH EoS. Note, that positive values of the depth increase downwards. Regions occupied by the outer crust, inner crust and core appear with different colors and labeled. The region occupied by the accreted material is plotted with a gray crosshatch pattern. The top axis shows the total mass of the NS after accretion, $M + \delta M$. Above $M = 2.25\ M_\odot$ the configuration is unstable and the object will collapse to a black hole.

[1] http://cococubed.asu.edu/code_pages/codes.shtml

the magnetic field trapped with the fluid may be buried into the NS crust, and depending on the conditions (accreted mass and magnetic field strength), the burial depth could be as deep as the inner crust. We study next the impact of magnetic fields in the vicinity of the NS, namely the magnetosphere, in the burial process.

5 MAGNETOSPHERE

5.1 Potential magnetospheric solution

For simplicity in the following discussion we use a *reference model* with the APRDH EoS and $M = 1.4M_\odot$. This model results in a a NS with coordinate radius $R = 12.25$ km. The effect of the EoS and the NS mass are discussed later in the text. Given that both the magnetosphere and the accreted material involve low energy densities compared with those inside the NS, the spacetime outside the NS can be regarded as non-self-gravitating and approximated by the Schwarzschild exterior solution.

The magnetosphere extends between the NS surface and the magnetopause, which will be assumed to be a spherically symmetric surface at the location of the infaling reverse shock. We model this region using the force-free magnetic field approximation, $\mathbf{J} \times \mathbf{B} = 0$, $\mathbf{J}$ being the electric current and $\mathbf{B}$ the magnetic field. We neglect the currents resulting from the rotation of the star. Consequently the magnetic field has a potential solution, solution of the relativistic Grad-Shafranov equation. In spherical coordinates, the magnetic field vector components are related to the vector potencial $\mathbf{A}$ as,

$$\hat{B}_r = \frac{1}{r^2 \sin\theta}\partial_\theta A_\phi \,, \tag{18}$$

$$\hat{B}_\theta = \frac{-1}{r^2 \sin\theta}\partial_r A_\phi \,, \tag{19}$$

$$\hat{B}_\phi = 0 \,, \tag{20}$$

where $\hat{B}_i = \sqrt{\gamma} B_i$ and γ is the determinant of the spatial metric. If we assume axisymmetry, the unique nonzero component of the electric current is the ϕ component,

$$J_\phi = \sin\theta \left[\partial_r(r\hat{B}_\theta) - \partial_\theta \hat{B}_r\right] . \tag{21}$$

Imposing the force-free condition, we obtain,

$$-J_\phi \hat{B}_\theta = 0 \,, \tag{22}$$

$$J_\phi \hat{B}_r = 0 \,. \tag{23}$$

Since $\hat{B}_r, \hat{B}_\theta \neq 0$, the only possible solution is $J_\phi = 0$. As we want an expression that only depends on the vector potential, we replace Eqs. (18) and (19) in equation (21) resulting in

$$\begin{aligned} J_\phi &= \sin\theta \left[\frac{-1}{\sin\theta}\partial_r(\partial_r)A_\phi - \frac{1}{r^2}\partial_\theta\left(\frac{\partial_\theta A_\phi}{\sin\theta}\right)\right] \\ &= -\partial_{rr}A_\phi - \frac{1}{r^2}\partial_{\theta\theta}A_\phi + \frac{\cot\theta}{r^2}\partial_\theta A_\phi = 0 \,. \end{aligned} \tag{24}$$

We discretize this expression using second order finite differences and solve the resulting linear system of equations using a cyclyc reduction algorithm (Swarztrauber 1974). We impose Dirichlet boundary conditions on A_ϕ at the surface of the NS to match with the interior value of the radial component of the magnetic field. Our aim is to describe a magnetosphere, which is confined within a certain radius, $R_{\rm mp}$, defining the magnetopause. Magnetic field lines at the magnetopause are parallel to this interface and they enter the NS along the axis. Therefore, they correspond to lines with $A_\phi = 0$, which we use as Dirichlet boundary condition at $R_{\rm mp}$ to solve the Grad-Shafranov equation. We can obtain the field distribution after the compression by simply changing the radius where the boundary conditions are imposed. The evolution of the magnetic field geometry before and after compression is shown in Fig. 3 for three illustrative cases.

For the interior magnetic field, which determines the boundary conditions at the surface of the star, we use two different magnetic field distributions, a dipolar magnetic field (*dipole* herafter) and a poloidal field generated by a circular loop of radius $r = 4 \times 10^5$ cm (Jackson 1962) (*loop current* hereafter). Following Gabler et al (2012), it is useful to introduce the *equivalent magnetic field*, B^*, which we define as the magnetic field strength at the surface of a Newtonian, uniformly magnetized sphere with radius 10 km having the same dipole magnetic moment as the configuration we want to describe. It spans the range $B^* \in [10^{10} - 10^{16}]$ G.

5.2 Magnetosphere compression

In the case of a fluid accreting onto a force-free magnetosphere, the magnetopause will remain spherical and will move inwards as long as the total pressure of the unmagnetized fluid, $p_{\rm tot} = p + p_{\rm ram}$, exceeds that of the magnetic pressure, $p_{\rm mag}$, of the magnetosphere. If we approximate the magnetopause as a spherical boundary between the spherically symmetric accreting solution described in Section 3 and the potential solution computed in Section 5.1, its properties can be described as the solution of a Riemann problem at the magnetopause. Since the magnetic field of the initial state is tangential to the magnetopause, we can use the exact solution of the Riemann problem developed by Romero et al. (2005). A succinct summary of the details of the implementation of the Riemann solver can be found in Appendix A.

For illustrative purposes the left panel of Fig. 4 shows the solution of the Riemann problem for a supersonic fluid accreting from the right into a magnetically dominated region (magnetosphere) on the left. The figure displays both the density (left axis, solid lines) and the fluid velocity (right axis, dashed lines). The initial discontinuity is located at $x = 0$. The right constant state of the Riemann problem corresponds to the accreting fluid with an entropy of $s = 10\ k_{\rm B}/{\rm nuc}$ and accretion rate of $\dot{M} = 10^{-7}\ {\rm M}_\odot/{\rm s}$. The left constant state corresponds a state with magnetic pressure $B^2/2$. The figure plots the corresponding solutions for different values of B around the equilibrium (indicated in the legend).

Looking at the left panel of Fig. 4 from left to right, the first jump in density corresponds to the contact discontinuity, point at which, as expected, the velocity remains continuos. The next discontinuity is a shock wave, where both the density and velocity are discontinuous, and both decrease. For low magnetic fields, $B \leqslant 10^{10}G$, the low magnetic pressure on the left state cannot counteract the total pressure of the accreting fluid and the contact discontinuity advances to the right at a velocity equal to that of the accreting fluid; a shock front is practically nonexistent. As the magnetic field is increased the velocity of the contact discontinuity decreases and it becomes zero at about $B = 10^{13}$ G. We identify this point as the *equilibrium point*, since no net flux of matter crosses $x = 0$. Around this equilibrium point, an accretion shock appears, which heats and decelerates matter coming from the right. The equilibrium point corresponds to a solution in which the matter crossing the shock has zero velocity, i.e. it piles up on top of the left state as the shock progresses to the right.

The actual accretion of matter onto a magnetically dominated magnetosphere is expected to behave in a similar way as the described Riemann problem. At large distances (low B) the mag-

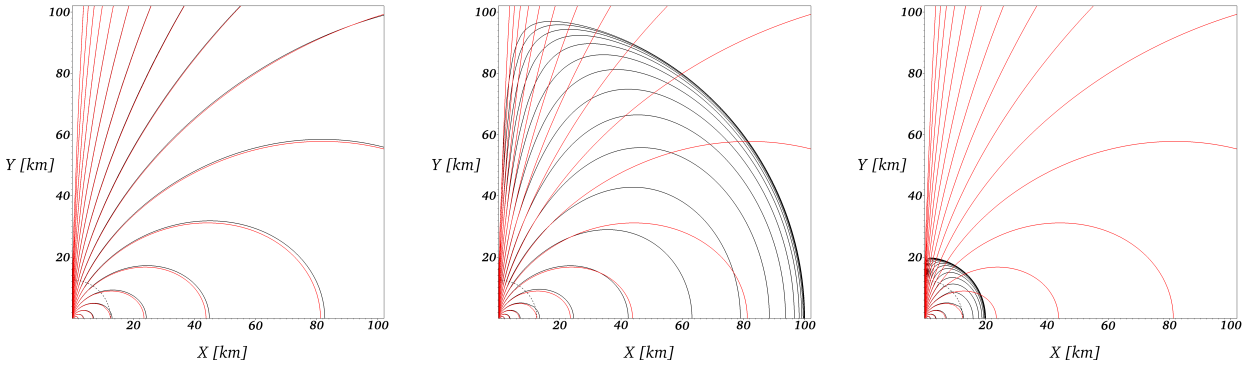


Figure 3. Magnetic field lines (black lines) for three different positions of the magnetopause for the same initial distribution of the magnetic field (red lines) with $B_p = 10^{13}$ G. The dashed line represents the NS surface.

netopause (contact discontinuity) is compressed at the speed of the fluid. As the magnetosphere is compressed, the magnetic field strenght raises and at some point an equilibrium point is found, beyond which the magnetosphere impedes the accretion of the fluid.

In the right panel of Fig. 4 we show for the sake of completeness the solution for a subsonic accreting fluid. In accreting NS this regime is probably unrealistic, since very large specific entropy is necessary ($s = 2000 k_{\rm B}/{\rm nuc}$ in the example plotted). In this case the solution is qualitatively different; instead of a shock, a rarefaction wave if formed for B below the equilibrium point. For larger values of B, an accretion shock is formed.

5.3 Setup

Our goal is to study the conditions under which the magnetic field of a new-born NS can be buried by fallback material during a supernova. We have spanned a large range of values for both, the magnetic field strength and the accretion rate, proceeding as follows. We obtain the distance from the NS surface where the magnetosphere and the accreting fluid are in balance, i.e. the radial point where the velocity of the contact discontinuity is zero. We reduce our 2D configuration to a 1D Riemann problem by restricting the evaluation of the equilibrium point to the equatorial plane of the NS, due to the fact that the magnetic pressure is maximum at the equator. Therefore, if the magnetic field can be buried in this latitude, it will be buried in all latitudes of the NS.

The code developed by Romero et al. (2005) requires as input the knowledge of the density, velocity, thermal pressure, and magnetic pressure at both left and right states of the initial discontinuity. In all cases we consider, the left state corresponds to the force-free magnetosphere while the right state is occupied by the accreting fluid. To obtain the magnetic pressure of the left state we find the solution of the Grad-Shafranov equation (see Section 5.1). This allows to locate the position of the magnetopause where the Riemann problem must be solved. Since the intertia of the fluid at the magnetosphere can be neglected in front of the magnetic pressure, the value of the density on the left state is set to yield an Alfvén velocity near to one , the thermal pressure is set to be at least six orders of magnitude lower than the magnetic pressure, and the velocity is set to zero. On the other hand, the values on the right state are fixed to the corresponding values of density, pressure and velocity of the stationary spherical accretion solution (see Section 3) and the magnetic pressure is set to zero.

A sketch of the different stages of the accretion process is shown in Fig. 5. The plots depict the location of the NS (including its core and inner and outer crust), the magnetosphere, the magnetopause, and part of the region where material is falling back. Each region is shaded in a different colour for a simple identification. Note that the scale ratio of the different regions is not preserved in the figure. The upper panel in Fig. 5 shows the initial state of the process. The panels on the left column show the expected evolution for a low magnetic field case (e.g. $B \lesssim 10^{13}$ G) while those on the right column correspond to a typical high magnetic field case (e.g. $B \gtrsim 10^{13}$ G). In general, the value of B separating between the two regimes depends on the accretion rate. For this figure we have chosen a value of the magnetic field that corresponds to a representative example of our results (see Section 6), for which $\dot{M} = 10^{-5} M_\odot/{\rm s}$. At the beginning of the evolution, the reverse shock falls over the magnetosphere. The magnetic field lines are confined inside the magnetosphere, which is shown in white on the diagram. Depending on the position of the sonic point, which in turn depends on the values of the specific entropy and the accretion rate, the motion of the reverse shock may be either supersonic or subsonic. We limit the qualitative description of the evolution below to the case of a supersonic reverse shock as in the subsonic case no accretion shock forms, as shown in Section 5.2.

The middle two panels in both evolutionary tracks show only qualitative differences in the size of the resulting magnetosphere after its compression and in the amplitude of the instabilities that may arise in the magnetopause (see below). Therefore, our description can be used for either path keeping this quantitative differences in mind. The evolution on the left column shows the case where the magnetic pressure is weak compared with the ram pressure of the fluid. In this case the magnetosphere shrinks significantly until the equilibrium point is reached ($R_{\rm mp}$; zero speed contact discontinuity) close to the NS surface at $R_{\rm s} \sim 10$ km. If the infall of the reverse shock is sxupersonic an accretion shock will appear simultaneously. The location of this accretion shock is shown on the horizontal axis of the four middle panels. As a result, the velocity of the reverse shock is reduced due to the presence of a region of subsonic accretion behind the accretion shock. Nevertheless, as through the accretion shock the momentum is conserved, the compression is not affected. The evolution on the right column, where the magnetic pressure is stronger, is qualitatively similar, only the

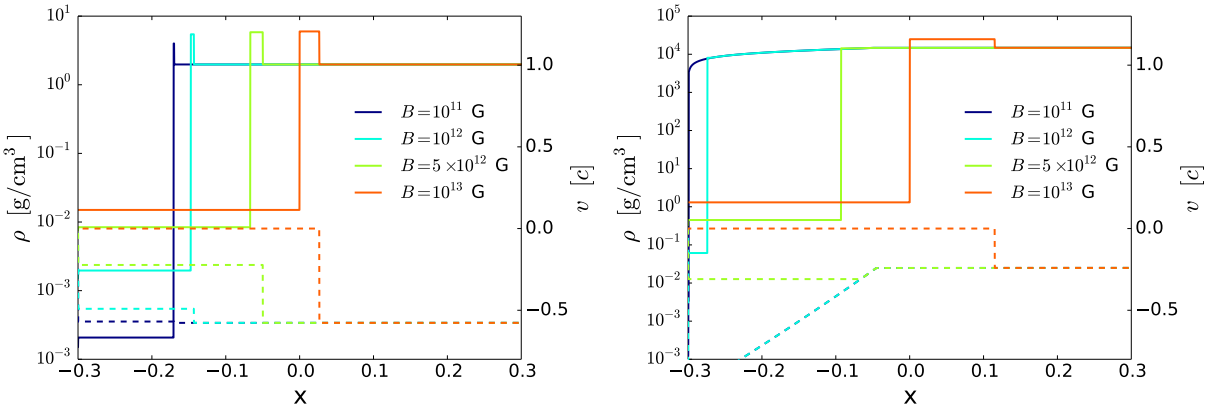


Figure 4. Density (solid lines, left axis) and velocity (dashed lines, right axis) profiles of the solution of the Riemann problem for several values of the magnetic field. Initially the discontinuity is set at $x = 0$, an accreting fluid at $x > 0$ and a magnetized fluid at $x < 0$, with constant magnetic field B. The left panel shows the case of supersonic accretion of a fluid with specific entropy $s = 10 k_{\rm B}/{\rm nuc}$ and $\dot{M} = 10^{-7}$ M$_\odot$/s at $t = 0.3$ s . The right panel shows the case of subsonic accretion of a fluid with $s = 2000 k_{\rm B}/{\rm nuc}$ and $\dot{M} = 10^{-5}$ M$_\odot$/s at $t = 0.3$ s.

accretion shock is located further away from the NS surface and the magnetosphere is not so deeply compressed.

As we will discuss below in more detail, the compression phase is unstable against the growth of Rayleigh-Taylor instabilities and the development of convection on the dynamic timescale. Therefore, the fluid and the magnetic field lines can mix, which provides a mechanism for the infalling fluid to actually reach the star. As the fluid reaches the NS, the mass of the star grows from $M_{\rm s}^*$ to $M_{\rm s}$ and its radius increases from $R_{\rm s}^*$ to $R_{\rm s}$, encompassing the twisted magnetic field lines a short distance away. The mass accreted δM forms part of the new crust of the NS, whose final radius will depend on the total mass accreted during the process. The bottom panels of the diagram depict a magnified view of the NS to better visualize the rearrangement the mass of the star and the magnetic field undergo. If the radius $R_{\rm mp}$ of the equilibrium point is lower than the new radius $R_{\rm s}$, all the magnetic field lines will be frozen inside the NS new crust, as shown in the bottom-left plot of Fig. 5 which corresponds to the end of the accretion process for a low magnetic field evolution. On the contrary, if the magnetic field is high, as considered on the evolutionary path on the right, the equilibrium point $R_{\rm mp}$ is far from the surface of the NS. Although part of the infalling matter may still reach the star and form a new crust, the mechanism is not as efficient as in the low magnetic field case. This is depicted in the bottom-right panel of the figure.

In our approach, that we discuss in more detail in the section on results, we compare the distance obtained by the Riemann solver for the location of $R_{\rm mp}$ (zero speed in the contact discontinuity) with the increment of the radius of the NS, δR, due to the pile up of the accreting matter. If the radial location of the equilibrium point $R_{\rm mp}$ is lower than δR (as in the bottom-left panel of Fig. 5) we conclude that the magnetic field is completely buried into the NS crust. On the contrary, if $R_{\rm mp} > \delta R$, our approach does not allow us to draw any conclusion. In this case, multidimensional MHD numerical simulations must be performed to obtain the final state of the magnetic field.

6 RESULTS

We turn next to describe the main results of our study. In order to be as comprehensive as possible, we cover a large number of cases which are obtained from varying the physical parameters of the model, namely the composition and entropy of the accreting fluid, the mass of the NS, and the initial magnetic field distribution. For all possible combinations of these parameters the outcome of the accretion process depends both on the magnetic field strength and on the mass accretion rate. This dependence is presented in the following sections in a series of representative figures. A summary of all the combinations considered and the description of the model parameters can be found in Table 2.

Table 2. Models considered in this study.

Model #	Composition	Entropy $k_{\rm B}/{\rm nuc}$	NS Mass M$_\odot$	MF distribution
Reference	He + NSE	10	1.4	loop current
1	He + NSE	100	1.4	loop current
2	He + NSE	1000	1.4	loop current
3	He + NSE	5000	1.4	loop current
4	He	10	1.4	loop current
5	He	100	1.4	loop current
6	He	1000	1.4	loop current
7	He	5000	1.4	loop current
8	C + NSE	10	1.4	loop current
9	C + NSE	100	1.4	loop current
10	C + NSE	1000	1.4	loop current
11	C + NSE	5000	1.4	loop current
12	He	10	1.4	dipole
13	He	1000	1.4	dipole
14	He	10	1.2	loop current
15	He	10	1.6	loop current
16	He	10	1.8	loop current
17	He	10	2.0	loop current

6.1 Reference model

We use as a reference model the one corresponding to an accreting fluid with $s = 10\ k_{\rm B}/{\rm nuc}$, and composed essentially by Helium. The nuclear reactions to reach nuclear statistical equilibrium are also allowed in this model. The mass of the NS is $1.4\ M_\odot$ and the magnetic field is generated by a *loop current* in the NS.



Figure 5. Sketch of the representative stages of the accretion process. The upper panel shows the initial state of the process. The left column shows the expected evolutionary path for a low magnetic field ($B \lesssim 10^{13}$ G) while the right column correspond to a typical high magnetic field case (e.g. $B \gtrsim 10^{13}$ G). A mass accretion rate of $10^{-5} M_\odot/\mathrm{s}$ is assumed. The scale ratio of the different regions is not preserved. See main text for details.

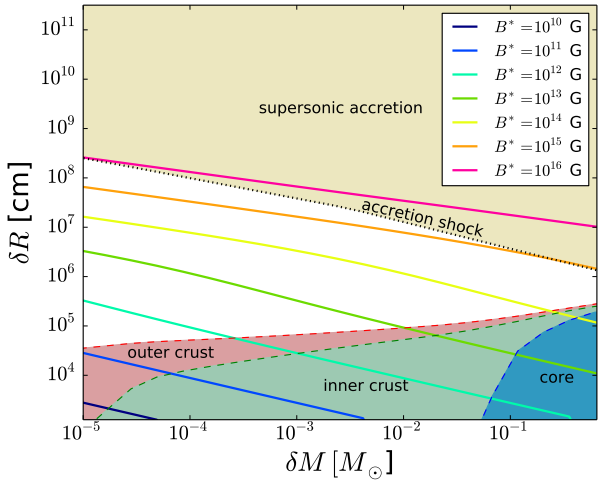


Figure 6. Distance above the star of the equilibrium point δR as a function of the total mass accreted δM for each value of the magnetic field (solid lines) for the reference model. The yellow area indicates the region where the accretion flow is supersonic. The dotted line represents the limit of the accretion shock. The red area marks the outer crust of the NS after accretion, while the green and blue areas display the inner crust and the core respectively, as shown in Fig. 5.

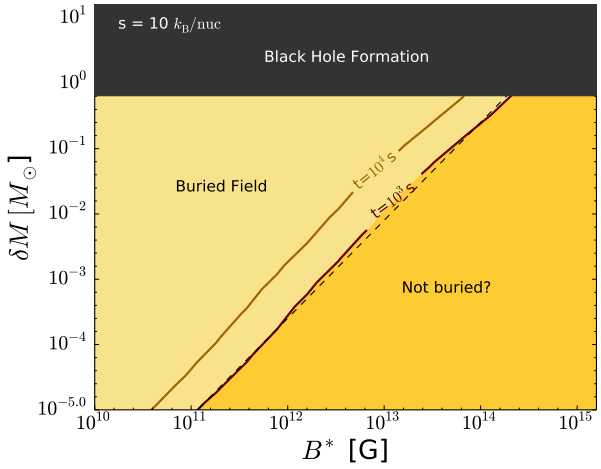


Figure 7. Outcome of the accretion depending on the total accreted mass (δM) and the initial magnetic field (B^*) for the reference model. For the two accretion times considered, $t = 10^3$ s (dark brown) and $t = 10^4$ s (light brown), the respective line splits the parameter space in a region where the magnetic field will be buried (left side) or not completely buried (right side). Above certain δM a black hole will be formed. The dashed line represents the fit shown in Eq. (25).

The results are shown in Fig. 6. The solid lines in this figure represent the distance of the equilibrium point δR (position of the magnetopause) above the NS surface as a function of the total accreted mass δM. The limit of the horizontal axis is given by the maximum mass that can be accreted without forming a black hole. Each line corresponds to a different value of the initial magnetic field, indicated in the legend of the figure. The yellow area represents the region in which the accretion of the reverse shock is supersonic and the black dotted line shows the limit of the accretion shock. The dashed red line shows the radial location of the new surface of the star due to the accretion of the infalling matter. The lines which cross the dashed red line have the equilibrium point inside the crust of the NS and, therefore, the corresponding magnetic fields will be buried into the crust. However, for the lines that are in the white area, the equilibrium point is not close enough to the NS surface and the magnetic field can not be buried. Note that for initial values of the magnetic field $B \gtrsim 10^{15}$ G, the magnetic field is never buried for all mass accretion rates considered.

An alternative view of this result is shown in Fig. 7. The goal of this representation is to provide a clearer representation of the dependence of the equilibrium point with the span of values of the magnetic field and the total mass accreted we are considering. The figure shows the isocontours where the equilibrium point is equal to the increment of the radius of the NS, i.e. $R_{\rm mp} = \delta R$. The two lines plotted (dotted, $t = 10^4$ s, and solid, $t = 10^3$ s) correspond to the limits of the total accretion time, which relates the accretion rate $\dot{M}$ and the total mass increment δM. The black area indicates the values of the maximum mass of the NS beyond which it will form a black hole. The dark orange region represents the span of values of δM and B^* where we cannot assure that the magnetic field could be buried completely. The light orange area, on the other hand, represents the cases where the magnetic field is totally buried. The results show that for low values of the magnetic field ($B^* < 10^{11} G$) the field can be buried even with the lowest accretion rates we have considered. As expected, as the accreted mass increases it is possible to bury the magnetic field for larger initial field values, up to a certain maximum. Indeed, for $B^* > 2 \times 10^{14}$ G we cannot find any accretion rate which can bury the magnetic field.

6.2 Models with higher specific entropy

We turn next to analyze the behavior of the magnetic field compression when the accreting fluid has higher specific entropy than in the reference model, keeping the same conditions for the composition, mass and magnetic field distribution (Models 1, 2 and 3 in Table 2). Fig. 8 shows the results for values of the specific entropy of $s = 100\ k_{\rm B}/{\rm nuc}$, $1000\ k_{\rm B}/{\rm nuc}$ and $5000\ k_{\rm B}/{\rm nuc}$ compared with the reference model ($s = 10\ k_{\rm B}/{\rm nuc}$). For the model with specific entropy $100\ k_{\rm B}/{\rm nuc}$, the results are very similar to the reference model as both lines almost perfectly overlap. For larger specific entropy the difference is more noticeable; for $s = 1000\ k_{\rm B}/{\rm nuc}$ and $5000\ k_{\rm B}/{\rm nuc}$, the burial/reemergence boundary of the parameter space is shifted toward larger magnetic fields, i.e. higher entropy material compress the magnetosphere more easily and it is possible to bury larger magnetic fields. This behavior can be understood if one considers that the equilibrium point is a balance between the total pressure of the infall material, $p_{\rm tot} = p + p_{\rm ram} \approx p + \rho v^2$, and the magnetic pressure of the magnetosphere. For low specific entropy, the total pressure is dominated by the ram pressure and changes in s do not produce significant changes in the equilibrium point. Above a certain threshold, the thermal pressure p dominates the total pressure and increasing s induces a larger compression of the magnetosphere, shifting the equilibrium point downwards. For realistic values of the specific entropy in supernovae, $s \sim 10 - 100\ k_{\rm B}/{\rm nuc}$ (Scheck et al 2006; Kifonidis et al. 2003, 2006), we expect the ram pressure to be dominant and hence the influence of s to be minimal. Even for an unrealistically large value of the specific entropy, $5000\ k_{\rm B}/{\rm nuc}$, the maximum magnetic field that can be buried increases one order of magnitude at most, and only for the largest mass accretion rates considered.

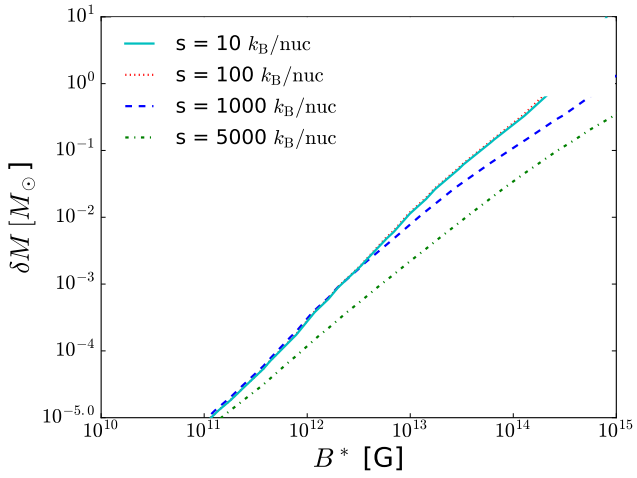


Figure 8. Similar to Fig. 7 but for the models with different specific entropy for the accreting fluid (namely, models 1 to 3 and reference). All cases are shown for a total accretion time of 10^3 s. Each line ends at the maximum mass of the corresponding model.

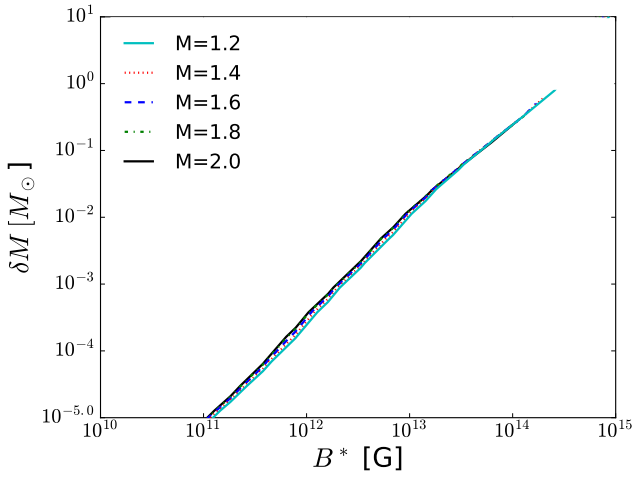


Figure 9. Similar to Fig. 7 for the models with different NS mass: 1.2 $M_\odot$, 1.6 $M_\odot$, 1.8 $M_\odot$, 2.0 $M_\odot$ (models 14, 15, 16 and 17 and reference). All cases are shown for a total accretion time of 10^3 s. Each line ends at the maximum mass of the corresponding model.

6.3 Models with different NS mass

We consider next the effect of the neutron star mass, within astrophysically relevant limits. According to observations (see Lattimer 2012, and references therein) the lower limit for the NS mass is around 1.2 $M_\odot$. The maximum achievable mass of a NS is strongly dependent on the equation of state (Lattimer & Prakash 2012). Nowadays, there are a few observations that support the existence of pulsars and NS with masses greater than 1.5 $M_\odot$, in particular an observation of a $\sim$ 2 $M_\odot$ NS (Demorest et al. 2010; Antoniadis et al. 2013). For this reason, we explore the results for several values of the neutron star mass between 1.2 $M_\odot$ and 2 $M_\odot$. The results are shown in Fig. 9, where each line corresponds to a model with different NS mass as indicated in the legend. The results for all masses are very similar. In general we observe that for more massive NS, a higher accreted mass is needed to bury the magnetic field. Our interpretation is that higher mass NS have lower radii and hence we have to compress more the magnetosphere to successfully bury it into the crust. Therefore, a higher accreted mass is needed to bury the field for NS with larger mass (smaller radius). Since the radius difference between a 1.2 and a 2 $M_\odot$ NS is small, the impact of the NS mass on the burial is minimal. The maximum value of the magnetic field which can be buried is $\sim 2 \times 10^{14}$ G in all cases. For smaller NS masses slightly larger values of the magnetic field can be buried due to the ability to support a larger accreted mass. We conclude that the burial of the magnetic field is not crucially sensitive to the NS mass.

6.4 Models with different EoS

Fig. 10 shows the comparison of the results for the reference model when using the four different equations of state described in section 4. For $M = 1.4\ M_\odot$, the coordinate radius of these NS models is 12.25 km for APRDH, 12.11 km for APRNV, 15.77 km for LDH and 15.37 km for LNV. Since the maximum mass is sensitive to the EoS, each line ends at different points in the δM vs B^* plot. The use of APRDH or APRNV EoSs leads to almost indistinguishable results (the two lines lay on top of each other). This is expected since the radius of this two models differs only by about

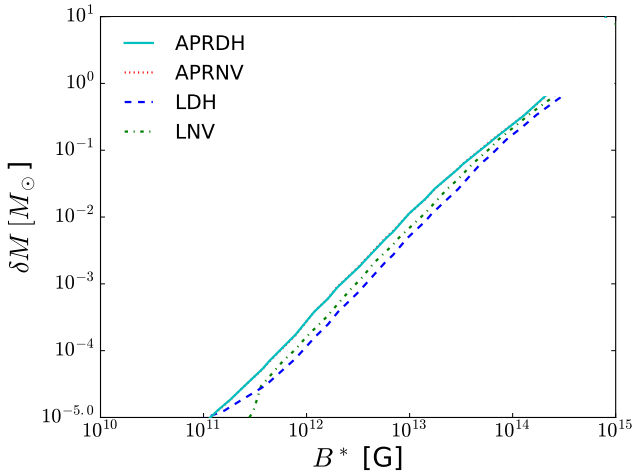


Figure 10. Similar to Fig. 7 for the models with different EoS, a NS of mass $1.4\mathrm{M}_\odot$ and specific entropy of the accreting fluid $10k_\mathrm{B}/\mathrm{nuc}$ All cases are shown for a total accretion time of 10^3 s. Each line ends at the maximum mass of the corresponding model.

1%, because the EoS are very similar and only differ at low densities (at the crust). The LDH and LNV EoSs allow the burial of a larger magnetic field for a given accreted mass, in comparison with APRDH and APRNV. The maximum magnetic field that can be buried in the LDH and LNV models is $\sim 6\times10^{14}$ G and $\sim 5\times10^{14}$ G respectively, which is about a factor 2 larger than for the APRDH EoS. In general, for a $M = 1.4\ M_\odot$, EoS resulting in a larger NS radius allow to bury larger magnetic fields for a given δM. Given that the results of this work are meant to be an order-of-magnitude estimate of the location in the parameter space of the limit between burial and reemergence, a difference of a factor 2 due to the EoS, does not change the main conclusions of this work. For practical purposes the APRDH EoS can be taken as a good estimator for this limit.

6.5 Remaining models

We do not observe any significant differences with respect to the reference model in the results for the models with different initial composition of the reverse shock (models 8 to 11) or the ones using the NSE calculations (models 4 to 7). As a result we do not present additional figures for these models since the limiting lines overlap with those of the reference model. The observed lack of dependence is due to the fact that the EoS only depends on the electron fraction, Y_e. This value is obtained from the ratio between the mean atomic mass number ($\bar{A}$) and the mean atomic number ($\bar{Z}$). For both cases of pure Helium and pure Carbon, this ratio is equal to $Y_e = 0.5$ and, consequently, the values of pressure and density for the accreting fluid are almost identical, producing differences in the results below the numerical error of our method [2]. In the case of the NSE calculation, the reason is similar. For low entropies ($s = 10, 100\, k_{\rm B}/{\rm nuc}$) the temperature is not sufficiently high to start the nuclear reactions and the composition remains constant throughout the accretion phase. For higher entropies, although the value of the electron fraction may differ from 0.5 during the accretion process, the differences produced in the thermodynamical variables lead to changes in the results of the Riemann problem still below the numerical error of the method.

Regarding the initial distribution of the magnetic field, we do not observe either any significant difference in the results in the two cases that we have considered, *loop current* and *dipole*. Given that we are comparing models with the same effective magnetic field, B^*, and thus the same magnetic dipolar moment, the magnetic field is virtually identical at long radial distances and the only differences appear close to the NS surface. In practice the magnetic field structure only changes the details of the burial in the cases in which the equilibrium point is close to the burial depth (the limiting line plotted in the Figs. 7 to 10), but it does not change the location of the limit itself in a sensitive way. As a conclusion, we can say that the dominant ingredient affecting the burial of the magnetic field is the presence of a dipolar component of the magnetic field but, for order-of-magnitude estimations, a multipolar structure of the field is mostly irrelevant.

7 SUMMARY AND DISCUSSION

We have studied the process of submergence of magnetic field in a newly born neutron star during a hypercritical accretion stage in coincidence with core collapse supernovae explosions. This is one of the possible scenarios proposed to explain the apparently low external dipolar field of CCOs. Our approach is based on 1D solutions of the relativistic Riemann problem, which provide the location of the spherical boundary (magnetopause) matching an external non-magnetised accretion solution with an internal magnetic field potential solution. For a given accretion rate and magnetic field strength, the magnetopause keeps moving inwards if the total (matter plus ram) pressure of the accreting fluid, exceeds the magnetic pressure below the magnetopause. Exploring a wide range of accretion rates and field strengths, we have found the conditions for the magnetopause to reach the equilibrium point below the NS surface, which implies the burial of the magnetic field. Our study has considered several models with different specific entropy, composition, and neutron star masses. Assuming an accretion time of 1000s, our findings can be summarised by a general condition, rather independent on the model details, relating the required total accreted mass to bury the magnetic field with the field strength. An approximate fit is (see dashed line in Fig. 7)

$$\frac{\delta M}{M_\odot} \approx \left(\frac{B}{2.5\times 10^{14}}\right)^{2/3}. \qquad (25)$$

The most important caveat in our approach is that we are restricted to a simplistic 1D spherical geometry, which does not allow us to consistently account for the effect of different MHD instabilities that can modify the results. We also note that our scenario is quite different from the extensively studied case of X-ray binaries, in which the NS accretes matter from a companion but at much lower rates (sub-Eddington) and matter is mostly transparent to radiation during accretion. In that case, matter cools down through X-ray emission during the accretion process. Davidson & Ostriker (1973) and Lamb (1973) already noticed this fact and predicted that the accretion will most likely be channeled through the magnetic poles, in analogy to the Earth's magnetosphere. In the context of X-ray binaries, Arons & Lea (1976) and Michel (1977) were able to compute equilibrium solutions with a deformed magnetosphere and a cusp like accretion region at the magnetic poles. However, as the same authors pointed out, these systems are unstable to the interchange instability (Kruskal & Schwarzschild 1954), a Raileigh-Taylor-like instabilitiy in which magnetic field flux tubes from the magnetosphere can raise, allowing the fluid to sink. This might allow for the formation of bubbles of material that fall through the magnetosphere down to the NS surface. In the case of a fluid deposited on top of a highly magnetized region, modes with any possible wavelength will be unstable (Kruskal & Schwarzschild 1954), however, in practice these instabilities are limited to the size of the magnetosphere ($\sim R_{\rm mp}$) in the angular direction. As the bubbles of accreted material sink, magnetic flux tubes raise, as long as their magnetic pressure equilibrates the ram pressure of the unmagnetized accreting fluid (Arons & Lea 1976). Therefore, in a natural way, the equilibrium radius computed in Section 5.2 roughly determines the highest value at which the magnetic field can raise.

This accretion mechanism through instabilities has been shown to work in the case of X-ray binaries in global 3D numerical simulations (e.g. Kulkarni & Romanova 2008; Romanova et al. 2008). In the case of the hypercritical accretion present in the supernova fallback, Rayleigh-Taylor instabilities have been studied by Payne & Melatos (2004, 2007); Bernal et al. (2010, 2013); Mukherjee et al (2013a,b). The simulations of Bernal et al. (2013) also show that the height of the unstable magnetic field over the NS surface decreases with increasing accretion rate, for fixed NS magnetic field strength, as expected. Using the method described in Section 5.2 we have estimated the equilibrium height over the NS surface for the 4 models presented in Fig. 9 of Bernal et al. (2013), for their lower accretion rates ($\dot{M} \leqslant 10^{-6}\ {\rm M}_\odot/{\rm s}$). Our results predict correctly the order of magnitude of the extent of the unstable magnetic field over the NS surface. Therefore, our simple 1D model for the equilibrium radius serves as a good estimator of the radius confining the magnetic field during the accretion process, although details about the magnetic field structure cannot be predicted. Another important difference with the binary scenario is the duration of the accretion process. In X-ray binaries, a low accretion rate is maintained over very long times, so that instabilities have always time to grow. In our case, hypercritical accretion can last only hundreds or thousands of seconds, and depending on the particular values of density and magnetic field, this may be too

[2] The numerical error is dominated by the calculation of the equilibrium point, which is computed with a relative accuracy of 10^{-4}.

short for some instabilities to fully develop. This issue is out of the scope of this paper and deserves a more detailed study.

Our main conclusion is that a typical magnetic field of a few times 10^{12} G can in principle be buried by accreting only $10^{-3} - 10^{-2} M_\odot$, a relatively modest amount of mass. This estimate has interesting implications: since it is likely that most neutron stars can undergo such an accretion process, and the field would only reemerge after a few thousand years (Geppert et al. 1999; Viganò & Pons 2012), the CCO scenario is actually not peculiar at all and we expect that most very young NSs show actually an anomalously low value of the magnetic field. On the contrary, magnetar-like field strengths are much harder to screen and the required accreted mass is very large, in some cases so large that the neutron star would collapse to a black hole. We also stress that the concept of *burial* of the magnetic field refers only to the large scale dipolar component, responsible for the magnetospheric torque spinning down the star. Small scale structures produced by instabilities can exist in the vicinity of the star surface, and this locally strong field is likely to have a visible imprint in the star thermal spectrum, as in Kes 79 (Shabaltas & Lai 2012), without modifying the spin-down torque. However, the high field burial scenario should not be very common because both, high field NSs are only a fraction to the entire population, and only a part of them would undergo the fallback episode with the right amount of matter. This is consistent with the recent results of Bogdanov (2014) who searched for the hidden population of evolved CCOs among a sample of normal pulsars with old characteristic ages but close to a supernova remnant. None of the eight sources studied was found to have a luminosity higher than 10^{33} erg/s, which would have been an evidence of a hidden strong field. They all show X-ray luminosities in the 0.3-3 keV band of the order of 10^{31} erg/s (or similar upper limits), consistent with the properties of other low field neutron stars with $B \approx 10^{12}$ G. Thus, these sample of sources are not likely to be linked to the family of descendants of Kes 79-like objects, but there is no contradiction with these being pulsars with reemerged normal fields. Finally, we note that the slow reemergence process on timescales of kyrs mimics the increase of the magnetic field strength, and it is therefore consistent with a value of the braking index smaller than 3 (Espinoza et al. 2011), which should be common for all young pulsars in this scenario.

ACKNOWLEDGMENTS

It is a pleasure to thank J.M. Martí for many fruitful discussions. This work has been supported by the Spanish MINECO grants AYA2013-40979-P and AYA2013-42184-P and by the Generalitat Valenciana (PROMETEOII-2014-069).

APPENDIX A: RIEMANN PROBLEM

For an ideal magneto-fluid, the energy-momentum tensor $T^{\mu\nu}$ and Maxwell dual tensor $F^{*\mu\nu}$ are

$$T^{\mu\nu} = \rho\hat{h}u^\mu u^\nu + g^{\mu\nu}\hat{p} - b^\mu b^\nu\,, \tag{A1}$$

$$F^{*\mu\nu} = u^\mu b^\nu - u^\nu b^\mu\,, \tag{A2}$$

where $\hat{h} = 1 + \varepsilon + p/\rho + b^2/\rho$ is the specific enthalpy including the contribution of the magnetic field and $\hat{p} = p + b^2/2$ is the total pressure. Moreover, b^μ stands for the magnetic field measured by a comoving observer (see Antón et al. (2006) for details and its relation with the magnetic field B^μ measured by a generic observer). The conservation of these two quantities, jointly with the conservation of the density current, equation (7), lead to the equations of ideal relativistic MHD.

$$\nabla_\mu J^\mu = 0\,, \tag{A3}$$

$$\nabla_\mu T^{\mu\nu} = 0\,, \tag{A4}$$

$$\nabla_\mu F^{*\mu\nu} = 0\,. \tag{A5}$$

In the particular configuration of our Riemann problem, $u^\mu = W(1, v^x, 0, v^z)$, $b^\mu = (0, 0, b, 0)$, so the term $\nabla_\mu b^\mu b^\nu$ in the conservation of the stress-energy tensor, vanish. Therefore, the conservation equations reduce to the purely hydrodynamical case.

The Riemann problem in this particular configuration is described in terms of three characteristics, one entropy wave and two fast magnetosonic waves. The initial problem with two states L (left) and R (right) breaks up into four states,

$$L\mathcal{W}_{\leftarrow} L_* \mathcal{C} R_* \mathcal{W}_{\rightarrow} R, \tag{A6}$$

where $\mathcal{W}$ indicate a fast magnetosonic shock wave or a rarefaction wave and $\mathcal{C}$ indicates the contact discontinuity. Solving the Riemann problem entails finding the intermediate states (L_*, R_*) and the position of the waves, which are determined by the pressure $\hat{p}_*$ and the flow velocity v^x_*. If $\hat{p} \leqslant \hat{p}_*$ the wave is a rarefaction wave (a self-similar continuous solution), otherwise the solution is a shock wave. In our case (see Romero et al. 2005) the ordinary differential equation that allows to obtain the solution for a rarefaction wave is given by

$$\frac{dv^x}{1-(v^x)^2} = \pm \frac{(1 + b^2/(\rho h c_s))\sqrt{\hat{h} + \hat{\mathcal{A}}^2(1-w^2)}}{\hat{h}^2 + \hat{\mathcal{A}}^2}\frac{dp}{\rho w}, \tag{A7}$$

where $\hat{\mathcal{A}} = \hat{h} W v^z$, $w = c_s^2 + v_A^2 - c_s^2 v_A^2$, $v_A = b^2/\rho\hat{h}$ is the Alfvén velocity and $c_s = \sqrt{\frac{1}{\hat{h}}\left.\frac{\partial p}{\partial \rho}\right|_s}$ is the sound speed. The integration of equation A7 allows to conect the states ahead (a) and behind (b) the rarefaction wave. Rarefaction waves conserve entropy, hence, all the thermodynamical variables and the differential of p must be calculated at the same entropy of the initial state. From this equation, the normal velocity behind the rarefaction can be obtained directly,

$$v^x_b = \tanh\hat{\mathcal{C}}, \tag{A8}$$

with

$$\hat{\mathcal{C}} = \frac{1}{2}\log\left(\frac{1+v^x_a}{1-v^x_a}\right) \pm \int_{\hat{p}_a}^{\hat{p}_b} \frac{(1 + b^2/(\rho h c_s))\sqrt{\hat{h} + \hat{\mathcal{A}}^2(1-w^2)}}{\hat{h}^2 + \hat{\mathcal{A}}^2}\frac{dp}{\rho w}. \tag{A9}$$

In the same way, the velocity inside the rarefaction can be obtained replacing the thermal pressure p by the total pressure $\hat{p}$.

On the other hand, shock waves should fulfill the so-called Rankine-Hugoniot conditions (Lichnerowicz 1967; Anile 1989)

$$[\rho u^\mu]\, n_\mu = 0\,, \tag{A10}$$

$$[T^{\mu\nu}]\, n_\nu = 0\,, \tag{A11}$$

$$[F^{*\mu\nu}]\, n_\nu = 0\,, \tag{A12}$$

where n_μ is the unit normal to a given surface and $[H] \equiv H_a - H_b$ being H_a and H_b the boundary values. The normal flow speed in the post-shock state, v^x_b, can be extracted from the Rankine-Hugoniot equations (see Romero et al. 2005, for a detailed discus-

sion),

$$v_b^x = \left(\hat{h}_a W_a v_a^x + \frac{W_s(\hat{p}_b - \hat{p}_a)}{j}\right) \quad \text{(A13)}$$

$$\times \left(\hat{h}_a W_a + (\hat{p}_b - \hat{p}_a)\left(\frac{W_s v_a^x}{j} + \frac{1}{\rho_a W_a}\right)\right)^{-1}, \quad \text{(A14)}$$

where $W_s = \frac{1}{\sqrt{1-V_s^2}}$ is the Lorentz factor of the shock,

$$V_s^{\pm} = \frac{\rho_a^2 W_a^2 v_a^x \pm |j|\sqrt{j^2 + \rho_a^2 W_a^2 (1 - v_a^x)^2}}{\rho_a^2 W_a^2 + j^2}\,, \quad \text{(A15)}$$

is the shock speed, and

$$j \equiv W_s \rho_a W_a (V_s - v_a^x) = W_s \rho_b W_b (V_s - v_b^x)\,, \quad \text{(A16)}$$

is an invariant derived directly from the Rankine-Hugoniot jump conditions. These expressions, together with the Lichnerowicz adiabat,

$$[\hat{h}^2] = \left(\frac{\hat{h}_b}{\rho_b} + \frac{\hat{h}_a}{\rho_a}\right), \quad \text{(A17)}$$

allows us to calculate the shock wave solution.

REFERENCES

Aguilera D., Pons J.A., Miralles J.A, 2008, A&A, 486, 255

Akmal A., Pandharipande V. R., Ravenhall D. G., 1998, Phys. Rev. C, 58, 1804

Anile A.M.,1989,*Relativistic Fluids and Magneto-Fluids; with Applications in Astrophysics and Plasma Physics.* Cambridge University Press.

Antón L., Zanotti, O., Miralles, J.A., Martí, J.M., Ibáñez, J.M., Font, J.A., Pons, J.A., 2006 ,ApJ, 637, 296

Antoniadis J. et al, 2013, Science, 340, 1233232

Arons J. , Lea S. M., 1976, ApJ, 207, 914

Bernal C.G., Lee W.H., Page D., 2010, RMAA, 46, 309

Bernal C.G., Lee W.H., Page D., 2013, ApJ, 770, 106

Bignami, G. F., Caraveo, P. A., De Luca, A., Mereghetti, S. 2003, Nature, 423, 725

Blondin J.M., 1986, ApJ, 308, 755

Bogdanov S., Ng C.-Y. and Kaspi V. M., 2014, ApJL, 792, L36

Bonanno A. et al., 2005, A&A, 440, 199

Burrows, A., Lattimer, J.M. , 1986, ApJ, 307, 178

Chevalier R.A. , 1989, ApJ, 346, 847

Janka, H.-T., Langanke, K., Marek, A., Martínez-Pinedo, G., MÏller, B., 2007, Phys. Rep., 442, 38

Colgate S.A. , 1971, ApJ, 163, 221

Davidson, K., Ostriker, J.P., 1973,ApJ 179, 585

De Luca, A., Mereghetti, S., Caraveo, P. A., Moroni, M., Mignani, R. P., Bignami, G. F. 2004, A&A, 418, 625

Demorest P. B., Pennucci T., Ransom S. M., Roberts M. S. E.,Hessels J. W. T., 2010,Nature, 467, 1081

Douchin F., Haensel P., 2001, A&A, 380, 151

Endeve E., Cardall C.Y., Budiardja R.D., Beck S.W. and Bejnood A., 2012 ApJ., 751, 26 (28pp)

Espinoza, C. M., Lyne, A. G., Kramer, M., Manchester, R. N., & Kaspi, V. M. 2011, ApJL, 741, L13

Faucher-Giguère, C.-A.; Kaspi, V. M., 2006, ApJ, 643, 332

Fryer, C. L. , 2006, New Ast. Rev., 50, 492-495

Geppert U., Page D., Zannias T., 1999, A&A, 345, 847

Goldreich P., Julian W.H., 1969, ApJ, 157, 869

Gotthelf, E. V., Halpern J.P., 2007, ApJL, 664, L35

Gotthelf E.V., Halpern J.P., Seward S.D., 2005, ApJL, 627, 390-96

Gotthelf E. V., Halpern J.P., Alford, J., 2013, ApJ, 766, id. 58

Goussard, J.-O.; Haensel, P.; Zdunik, J. L., 1998, A&A, 330, 1005

Gullón, M.; Miralles, J. A.; Viganò, D.; Pons, J.A., 2014, MNRAS, 443, 1891

Hammer N.J., Janka H.-Th., Müller E., 2010, ApJ, 714, 1371

Halpern, J. P., Gotthelf, E. V., Camilo, F., Seward, F. D. 2007, ApJ, 665, 1304 (Paper 2)

Halpern, J. P., Gotthelf, E. V., Camilo, F., Seward, F. D. 2010, ApJ, 709, 436

Helfand D.J, Becker R.H., 1984, Nature, 307, 215

Ho W.C.G., 2011, MNRAS, 414, 2567

Houck J.C., Chevalier R.A., 1991, ApJ, 376, 234

Hui, C. Y., Becker, W. 2006, A&A, 454, 543

Jackson, J. D. 1962, *Classical electrodynamics*, New York: Wiley.

Gabler M., Cerdá-Durán P., Font J.A., Müller E, Stergioulas N. , 2012, MNRAS, 430, 1811

Joggerst C.C, Almgren A., Woosley S.E.,2010, ApJ, 723, 353

Kifonidis K., Plewa T., Janka H.Th., Müller E., 2003, A&A, 408, 621

Kifonidis K., Plewa T., Scheck L., Janka H.Th., Müller E., 2006, A&A, 453, 661

Kruskal, M., Schwarzschild, M. 1954, Proc. R. Soc. A, 223, 348âĂŞ360

Kulkarni, A. K., Romanova, M. M., 2008, MNRAS, 386, 673

Lattimer J., Prakash M., 2005, Phys. Rev. Lett. 94, 111101

Lattimer J., 2012, Annual Review of Nuclear and Particle Physics, Vol. 62, 485

Lamb, F. K., Pethick, C. J., Pines, D. 1973, Astrophysical Journal, 184, 271

Lichnerowicz A.,1967, *Relativistic Hydrodynamics and Magnetohydrodynamics.* Benjamin.

Lorimer D. R., Kramer M., 2004, *Handbook of Pulsar Astronomy*, Cambridge University Press.

Mereghetti, S., De Luca, A., Caraveo, P. A., Becker, W., Mignani, R., Bignami, G. F. 2002, ApJ, 581, 1280

Michel F.C., 1972, Ap. Space Sci., 15, 153

Michel F.C., 1977, ApJ, 214, 261

Mukherjee, D., Bhattacharya, D., Mignone, A. 2013, ApJ, 430, 1976

Mukherjee, D., Bhattacharya, D., Mignone, A. 2013, ApJ, 435, 718

Muslimov A., Page D., 1995, ApJ , 440, L77

Negele J. W., Vautherin D., 1973, Nuclear Physics A, 207, 298

Obergaulinger M., Janka H.T., Aloy-Torás M. A., 2014, MNRAS, 445, 3169

Pandharipande V. R., Smith R. A., 1975, Physics Letters B, 59, 15

Page, D., Lattimer J.M., Prakash M., Steiner, A.W., 2004, ApJS, 155, 623

Payne, D. J. B., Melatos, A. 2004, ApJ, 351, 569âĂŞ584

Payne, D. J. B., Melatos, A. 2007,ApJ, 376, 609âĂŞ624

Pons J.A., Geppert U., 2007, A&A, 470, 303

Pons J.A., Miralles, J.A., Geppert U., 2009, A&A, 496, 207

Pons J.A., Reddy S., Prakash M., Lattimer J.M., Miralles J.A., 1999, ApJ, 513, 780

Romanova M. M., Kulkarni A. K., Lovelace, Richard V. E, ApJL, 673, L171.

Romero R., Martí J.M, Pons J.A., Ibáñez J.M., Miralles J.A., 2005, J. Fluid Mech., 544, 323-338

Seitenzahl R. et al., 2008, ApJ, 685, L129

Seward, F. D., Slane, P. O., Smith, R. K., Sun, M. 2003, ApJ, 584, 414

Shabaltas N. Lai D., 2012, ApJ 748, 148
Shapiro S.L., Teukolsky S.A., 2004, *Black holes, white dwarfs and NSs*, Wiley-VCH.
Scheck L., Kifonidis K., Janka H.-Th., Müller E., 2006, A&A 457, 963
Swarztrauber, 1974, SIAM J. Numer. Anal. 11, 1136-1150
Thompson C., Duncan R.C., 1993, ApJ, 408, 194
Timmes F.X, 1999, ApJ Supp. ser., 124, 241-263
Timmes F.X., Arnett D., 1999, ApJ Supp. Ser., 125, 277-294
Timmes F.X., Swesty D., 2000, ApJ Supp. Ser., 126, 501-516
Turolla R., Esposito P., 2013, Int. J. Mod. Phys., D, 22, 1330024
Viganò D., Pons J.A., 2012, MNRAS, 425, 2487-2492
Viganò D., Rea, N.; Pons, J. A.; Perna, R.; Aguilera, D. N.; Miralles, J. A., 2013, MNRAS, 434, 123
Ugliano M., Janka H.T., Marek A., Arcones A., 2012, ApJ, 757, 69
Woosley S.E., Weaver T.A., 1995, ApJ Supp. Ser, 101, 181
Woosley S.E., Heger A., Weaver T.A., 2002, Rev. Mod. Phys., 74, 1015
Wongwathanarat A., Müller E., Janka H.-Th., 2015, A&A, 577, A48
Young E.J., Chanmugan G., 1995, ApJ, 442, L53
Zavlin V.E., Pavlov G.G., Sanwal D., Trumper J., 2000, ApJL, 540, L25
Zhang W., Woosley S.E., Heger A., 2008, ApJ, 679, 639